

# Laser Cladding of NiCrMoFeNbTa Particles on Inconel 625 Alloy: Microstructure and Corrosion Resistance

N. Jeyaprakash<sup>1</sup>  · Che-Hua Yang<sup>1</sup> · P. Susila<sup>2</sup> ·  
Sundara Subramanian Karuppasamy<sup>1</sup>

Received: 24 March 2022 / Accepted: 15 July 2022 / Published online: 1 November 2022  
© The Indian Institute of Metals - IIM 2022

**Abstract** The objective of this study is to analyse the anti-corrosion characteristics of NiCrMoFeNbTa powder particles cladded on the Inconel 625 alloy. The microstructure and hardness of the NiCrMoFeNbTa cladded layer were evaluated by means of FESEM and nanoindentation techniques. At various time intervals (0, 18, 42 and 70 h), the anti-corrosion behaviour was investigated on IN 625 substrate and cladded specimens. In addition, the average surface roughness (Ra) value was obtained for the substrate and clad specimens to interrogate their resistant behaviour. The FESEM results proved the presence of cellular structure with interdendritic phases in the cladded region, and these phases improved the hardness at the clad layer compared to the substrate. The passive film formed on the NiCrMoFeNbTa cladded layer was reported to be compact and stable which resisted corrosion to a greater extent than the IN 625 substrate samples. On comparing the substrate and cladded samples, the unexposed clad specimen provided maximum corrosion resistance in terms of lower current density, higher polarization resistance and lower surface roughness values.

**Keywords** Inconel 625 cladding · Microstructure · Nanohardness · Corrosion · Surface roughness (Ra) · EIS analysis

## 1 Introduction

Surface engineering has changed the traditional ways of repairing the surface of the components. It involves many techniques that can rebuild or treat damaged surfaces by depositing the materials on the surfaces. This deposited film will enhance the mechanical characteristics, thereby aids in improving the durability of components. These methods eliminate the necessity for the new parts since the new parts are very expensive and thus can save money and time. Also, these methods are more preferred in applications employed in hostile environments [1–4]. Some of the widely used traditional techniques are thermal spraying, chemical vapour deposition (CVD), electrodeposition, physical vapour deposition (PVD), hardfacing, etc. These conventional techniques have their limitations. The controllability and repeatability of the electro and vapour deposition process are tricky [5, 6]. On the other hand, the thermal spray process can have a better bonding behaviour and repeatability compared with the deposition process. But this process is not effective for smaller and curved substrates due to the low degree of adhesion. In some applications, because of the heat-affected zone (HAZ), a series of problems arise after long-term usage [7]. The hardfacing technique involves repairing worn-out surfaces by recreating them and thereby improving the working life. However, the distortion effect produced by the high-temperature arc greatly limits the usage of this technique [8]. The drawbacks of the traditional techniques have been overcome by the laser surface treatments.

✉ N. Jeyaprakash  
prakash84gct@gmail.com

✉ P. Susila  
susilaiitm@gmail.com

Che-Hua Yang  
chyang@ntut.edu.tw

Sundara Subramanian Karuppasamy  
diwaha3@gmail.com

<sup>1</sup> Graduate Institute of Manufacturing Technology, National Taipei University of Technology, Taipei 10608, Taiwan

<sup>2</sup> Department of Mechanical Engineering, College of Engineering Guindy, Anna University, Chennai, Tamil Nadu 600025, India

Laser surface treatments (LST) involve a high-energy laser that melts the substrate's surface. LST can be applied to materials with any geometry, being able to produce excellent bonding behaviour with the substrates, rapid, eco-friendly, highly efficient and capable of creating coatings with high precision [9–12]. These advantages have paved the way for implementing LST to improve the tribological properties of components that are employed in severe aggressive environments [13, 14]. Among the various methods of LST, the laser cladding process is mostly preferred for treating worn-out surfaces with greater accuracy. The coating material is directly deposited on the metal pool at a uniform rate, thereby producing an even film of the coated layer. It can create effective thick coatings and is majorly employed in repairing the components of nuclear reactors, turbine blades, boiler tubes, pressurized water reactors, steam turbines, etc., which operate in harsh environments [15–17].

Nickel-based superalloys are designed for high-temperature applications since these alloys resist heat even near to their melting point. It is a combination of nickel with chromium, molybdenum, iron and other refractory elements which makes it resistant to high temperatures. Considering the design aspects, these alloys exhibit better values of thermal conductivity, low density, elastic modulus and are cost effective [18–20]. NiCrMoFeNbTa alloy (Inconel 625) is a nickel-based superalloy that is obtained due to the solid solution strengthening effect of Mo and Nb in the Ni–Cr matrix. In addition, these alloys exhibit better fatigue strength, higher hardness, greater tensile properties and ductility, and provide resistance against local corrosion attacks in intrusive environments [21, 22]. The adequate composition of Mo (~ 10%) resists crevice and pitting type of corrosion [23]. These features made the IN 625 alloy get well adapted for a wide range of applications in furnace hardware, chemical plants, space shuttle engines, heat exchangers, control rods, gas turbines, seawater equipments, etc. [24]. Surface treatment using the laser cladding process will be a better option for improving the anti-corrosion behaviour and other mechanical properties of IN 625 components. The choice of the coating material is important as it is required to sustain in those environments and also it has to aid in improving durability. Since higher Cr content provides stable passive film during corrosion, the substrate material is preferred as the cladding material (IN 625).

D. Viridi et al. [25] analysed the hardness of Inconel 625 coating produced using laser cladding. Tai-Cheng Chen et al. [26] studied the wear behaviour of thermally sprayed IN 625 films and reported that the formed coating was very stable and provided better wear resistance compared with the carbon steel. Z. Liu et al. [27] and H.Y.Al-Fadhli et al. [28] examined the corrosion and erosion-corrosion behaviour of

High Velocity Oxygen Fuel (HVOF) sprayed IN 625 coating and reported that IN 625 exhibits better resistance towards erosion and corrosion than the base samples. Tai-Cheng Chen et al. [29] compared the tribological behaviour of IN 625 coatings and found that the IN 625 coatings experienced reduced wear rate, low coefficient of friction, better hardness and corrosion-resistant property. Thus, from the literature, it is evident that IN 625 will be an appropriate choice of cladding material for improving the tribological properties of the critical components. This study is aimed to evaluate the anti-corrosion of the Inconel 625 coating on the IN 625 substrate. The microstructure and hardness of the IN 625 coatings were investigated. At various time periods (0, 18, 42 and 70 h), the anti-corrosion behaviour was investigated on the IN 625 and clad specimens in an electrochemical workstation for interrogating the resistance they offered against corrosion. After the corrosion analysis, the corroded morphology of the specimens was analysed with the aid of FESEM and EDS analysis. Moreover, the polarization resistance values were compared to further evaluate the resistance offered. Surface roughness was evaluated on the substrate and clad samples in response to the corrosion resistance. The results of all analyses have been compared, presented and the values tabulated.

## 2 Experimentation

### 2.1 Materials and Laser Cladding

Figure 1a represents the morphology of the as-received NiCrMoFeNbTa (IN 625) powder particles. From this figure, the average size of the IN 625 alloy particles is found to be  $100 \pm 25 \mu\text{m}$ . The elemental composition of the IN 625 material is tabulated in Table 1. Inconel 625 is selected as the substrate material. IN 625 substrate's surface was rinsed by cleaning agents like acetone and then sandblasted. The sandblasting process was performed on the rinsed samples. The surface roughness of the sand-blasted samples was found to be  $\sim 6 \mu\text{m}$ . After these pre-processing steps, the cladding process was executed as depicted in Fig. 1b. The process parameters like gas flow rate (shield and carrier gas), laser power, scanning speed, powder feed rate, etc. will decide the cladding powder distribution and the thickness of the clad layer. The optimized process parameter used during cladding is tabulated in Table 2 [30]. This laser beam heated the surface, thereby creating the molten metal pool [31]. The NiCrMoFeNbTa alloy particles reached this pool via a coaxial feeder system. These particles got settled in the metal pool which tended to the formation of a finite layer of IN 625 particles on IN 625 substrate [32]. The clad

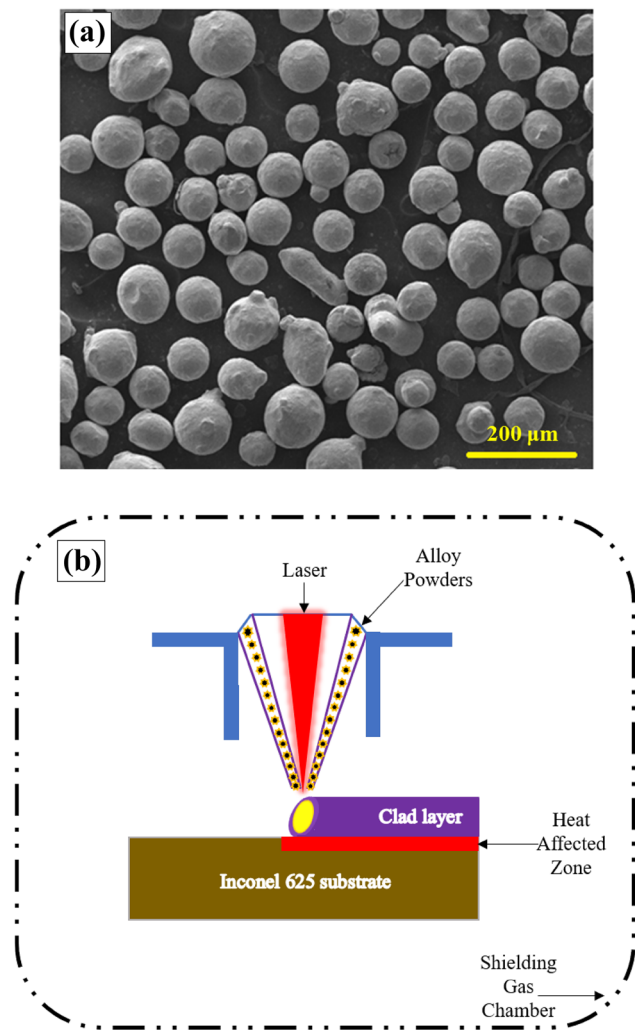


**Fig. 1** a FESEM picture of as-received NiCrMoFeNbTa (IN 625) particles, b Schematic representation of the laser cladding process

samples were collected, and some post-processing procedures were carried out for investigating the morphology of the clad layer. The chemical etching process was performed on the diamond polished clad surface to evaluate the microstructure at the clad layer.

**2.2 Corrosion Test**

After the cladding process, the substrate and clad samples underwent corrosion tests at 0, 18, 42 and 70 h to evaluate

the resistance they offered against corrosion. The corrosion test was performed in an electrochemical workstation. This workstation consisted of a three-electrode assembly namely the Pt, AgCl and the working electrode (sample). The electrolytic solution was prepared by dissolving 3.5% wt of sodium chloride crystals in 100 ml of DI water. This solution was the same as the chloride content in ocean water and was able to induce severe corrosion attacks on the surface [33]. As per the ASTM G44-99 standards, the test samples were prepared and pre-processed before the corrosion test. First, the test samples were cleaned with acetone to remove the surface dust and with the help of SiC sheets, the rinsed samples were abraded and again cleaned with acetone for performing the corrosion test. The substrate and clad samples were immersed in the NaCl solution for the total duration of 70 h, and the corrosion test was performed at 0, 18, 42 and 70 h. After stabilizing the potential and changing the scan rate, the corrosion process was performed on the samples. The Tafel plots were obtained for the IN 625 substrate and clad samples and the corresponding current density and electrode potential values were tabulated. The corroded morphology of the samples was analysed to reveal the passive film formation along with the corresponding elemental mapping using the EDS spectra. Moreover, impedance analysis was also performed to further interrogate the sample’s corrosion resistance. The polarization resistance values were calculated using the equilibrium circuit, tabulated and compared. The surface roughness of the samples before and after the corrosion test was evaluated by means of images captured using the Scanning Probe Microscope (SPM) and laser microscope.

**3 Results and Discussion**

**3.1 Microstructural Examination**

Figure 2a represents the optical microscopic image captured at the clad layer. The captured image shows that the NiCrMoFeNbTa alloy was coated evenly on the IN 625 substrate and the clad layer is free from voids and other defects. This fine deposition is because of the optimized process parameters during the cladding process [30, 34]. In addition, the optical micrographs show that the clad layer consists of cellular dendritic microstructures. Figure 2b shows that the clad layer is said to be rich

**Table 1** Elemental composition of IN-625 alloy

Material	Ni (%)	Co (%)	Cr (%)	Fe (%)	Nb + Ta (%)	Si (%)	C (%)	Mn (%)	Mo (%)	Ti (%)	Al (%)
IN-625	REM	1.00	23.00	5.00	4.15	0.50	0.10	0.50	10	0.4	0.4

**Table 2** Laser parameters used for cladding process [30]

Material	Power	Feed rate	Scanning speed	Preheat temperature	Shielding gas flow	Carrier gas flow
IN625	1000 W	4 g/min	400 mm/min	150 °C	25 L/min	6 SD @ 100,000/Pa

in cellular/dendritic structures with interdendritic phases. These phases are distributed in the  $\gamma$ -nickel matrix [35]. This fine formation of cellular microstructure in the clad region is due to the rapid solidification effect after the cladding process [36]. The magnified view of Fig. 2b is shown in Fig. 2c. From this, it is evident that there is a segregation of interdendritic secondary phases in the  $\gamma$ -nickel matrix. Since the NiCrMoFeNbTa alloy contains notable percentages of niobium and molybdenum, during solidification, the  $\gamma$  phase (dendritic) is formed first, followed by the precipitation of interdendritic phases, due to the effect of niobium and molybdenum. Mostly, these secondary phases are rich in carbides of Nb, Cr and Mo

throughout their microstructure [37–39]. Figure 2d shows the point scan image (inset) used for EDS analysis along with the elemental graph obtained at the clad layer. From this elemental graph, it is found that the highest peak is obtained for nickel followed by chromium and other elements. Since, the substrate and the cladding material are nickel-based superalloys which constitute for higher elemental peaks for the nickel element. The Nb and Mo elemental peaks are observed in this graph which proves the existence of secondary interdendritic phases. Moreover, the elemental concentrations (wt%) of Ni, Cr, Mo, Nb, and Fe were measured and the values are 69.27, 18.85, 6.40, 3.73 and 1.75, respectively.

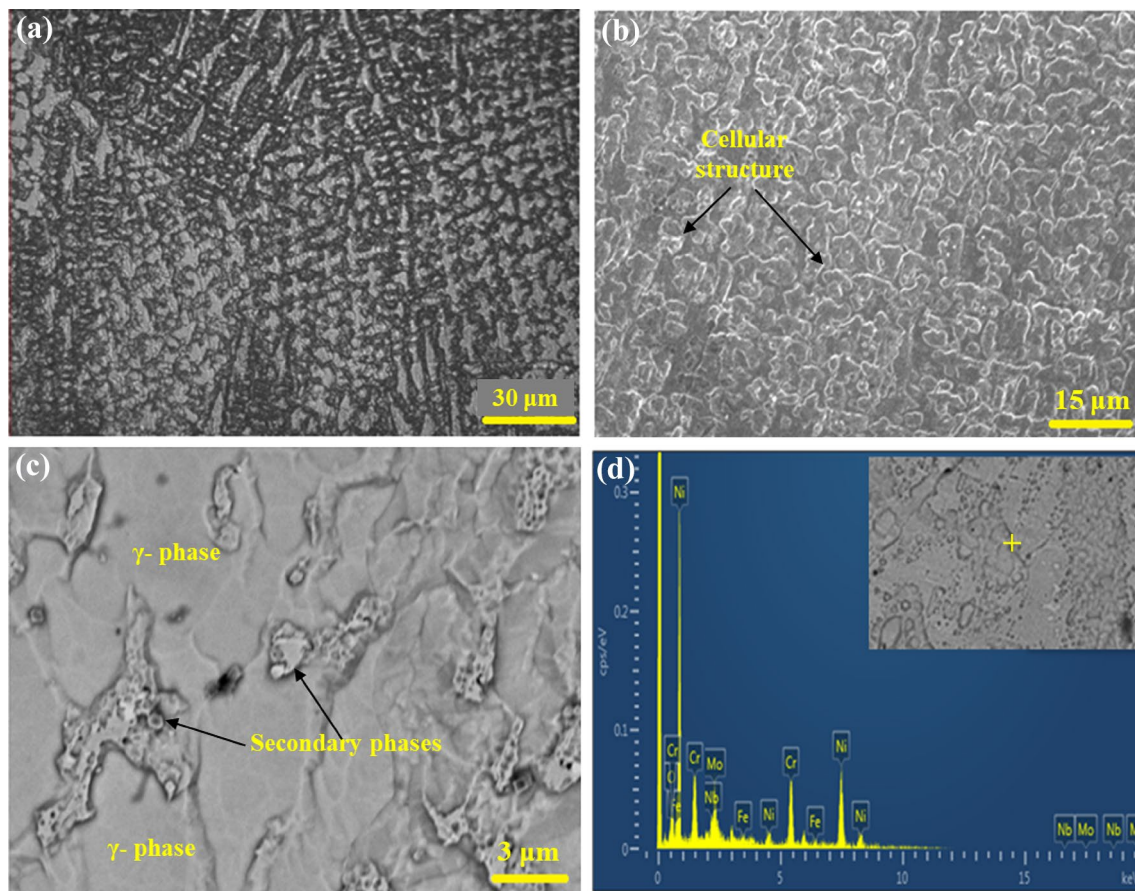


**Fig. 2** **a** Optical microscopic (OM) image of the clad region, **b** FESEM image of the clad sample representing the cellular structure, **c** Magnified view of **b**, and **d** EDS graph in the clad region (Inset: Image used for EDS scan)

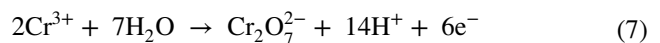
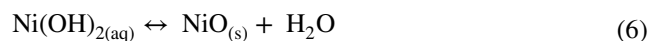
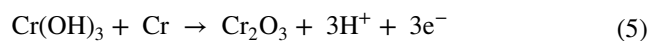
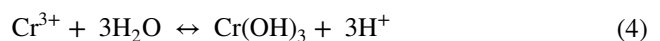
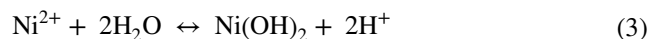
### 3.2 Nanohardness Evaluation

The material with greater hardness is reported to provide better wear resistance [40, 41]. A constant load of 1500  $\mu\text{N}$  was applied by the diamond probe followed by the unloading process, leaving the plastic deformation [42]. Figure 3a represents the optical microscopic image used for the nanoindentation test. It shows the substrate, interface and cladded regions after the cladding process. In Fig. 3b, the indentation depth is plotted against the applied load. In general, the indentation depth is in inverse relationship with the hardness offered. Greater indentation depth will result in lower hardness [43]. From Fig. 3b, it can be inferred that the substrate has a greater value of indentation depth ( $\sim 83$  nm) compared to the values obtained in the interface ( $\sim 60$  nm) and the cladded ( $\sim 41$  nm) layer. The depth value at the clad layer is one-half of the substrate's indentation depth value. The nanohardness value of the substrate, interface and the clad layer are 2.57, 3.02 and 4.39 GPa, respectively. On comparing the hardness values, the clad layer exhibits higher hardness than the interface and the substrate layers due to its lower indentation depth. The hardness value obtained in the clad layer is nearly twice the substrate's hardness value. This is because of the precipitation of Nb- and Cr-rich carbides as the secondary phases in the cladded region [44–46]. These precipitates are responsible for improving the hardness at the clad layer.

### 3.3 Corrosion Test

The major application of IN 625 alloy is in hostile environments experiencing severe corrosion attacks. The fuel tanks of the biomass reactors are reported to contain precipitates of chloride and sulphide. These precipitates readily react

with the IN 625 alloy resulting in the initiation of corrosion attacks, thereby reducing the corrosion-resistant behaviour [47]. In the case of supercritical boilers, pitting corrosion was observed on the Inconel 625 surface due to the salt deposits which may turn into corrosive acids after long-term use [48]. Mostly at elevated temperatures, the chromium present in the IN 625 alloy is oxidized to dichromate which can readily react with the formed passive film and thus minimize the resistance [49]. The reaction that accounts for the corrosion in Inconel 625 alloy is represented in Eqs. (1–7) [50].



The polarization curves obtained from the corrosion test of the substrate and the cladded specimens were expressed in terms of the Tafel plot as in Fig. 4a and b. The current density ( $I$ ) is plotted against the electrode potential ( $V$ ) and the current remains constant even after increasing the potential. No active to passive transitions have been reported, which proves that there is a continuity in the formation of oxide film on the samples. The measured  $V$  and

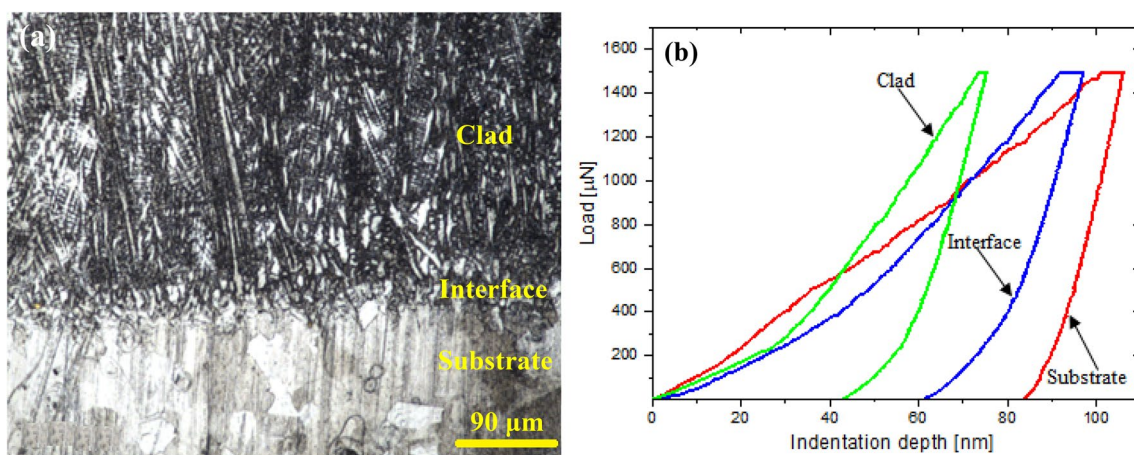


**Fig. 3** a OM image used for nanoindentation test representing the three regions, (b) Load to depth plot at the three regions

I value for the substrate and clad samples at 0, 18, 42 and 70 h are tabulated in Table 3. In general, lower the value of I, higher the corrosion resistance offered [51, 52]. From this table, among the IN 625 base samples, the 70 h sample has the minimum value of I ( $2.363 \times 10^{-7}$  A/cm<sup>2</sup>). An increasing trend is observed in the I value of 0, 42, and 18 h substrate samples, respectively. Hence, the oxide layer developed on the 70 h sample is said to be stable and provides better corrosion resistance. The clad samples have been reported to exhibit lower current densities and potential values than the IN 625 base samples. The precipitation of the interdendritic phases in the  $\gamma$ -Ni matrix accounts for the compact and stable passive film formation at the clad surface. These precipitates resist corrosion to a better extent, thereby improving the corrosion resistance property. On comparing the current density values from Table 3, the unexposed clad sample has the lowest value ( $6.145 \times 10^{-8}$  A/cm<sup>2</sup>) and offers greater corrosion resistance than the other clad and substrate samples.

The corroded morphologies and the elemental graphs of the IN 625 substrate samples at different intervals are shown in Fig. 5a–h. From the FESEM image of the substrate samples, the oxide film formed on the 70 h sample is more stable than the films of other substrate samples. The other sample’s passive film is greatly affected by the Cl<sup>-</sup> ions present in the test solution which react with the film and form pits during the corrosion process. Figure 6a–h represents the FESEM images and EDS maps of the clad samples at 0, 18, 42, and 70 h, respectively. It can be seen that all the clad samples have better film morphology due to the existence of cellular structures containing interdendritic carbide phases distributed in the  $\gamma$ -Ni matrix. These precipitates will withstand the corrosion attacks forming a strong passive film. Among the clad samples, the unexposed clad sample has compact and stable film formation and thus offers maximum

**Table 3** Corrosion test data

Duration	E- current (V)	I- current (A/cm <sup>2</sup> )
Substrate 0 h	-0.220	$2.892 \times 10^{-7}$
Substrate 18 h	-0.188	$3.780 \times 10^{-7}$
Substrate 42 h	-0.181	$3.229 \times 10^{-7}$
Substrate 70 h	-0.163	$2.363 \times 10^{-7}$
Clad 0 h	-0.129	$6.145 \times 10^{-8}$
Clad 18 h	-0.119	$1.624 \times 10^{-7}$
Clad 42 h	-0.123	$1.415 \times 10^{-7}$
Clad 70 h	-0.184	$6.651 \times 10^{-8}$

resistance against corrosion than other clad and substrate samples. The elemental compositions obtained from the elemental graphs of the substrate and clad samples are listed in Table 4. Figure 7 depicts the passive film formation on the NiCrMoFeNbTa clad layer.

**3.4 Electrochemical Impedance Spectroscopy Analysis**

The polarization curves show that the clad samples have better anti-corrosion behaviour due to their low I values. To further confirm these results, impedance analysis was carried out and the results were plotted as the Nyquist and Bode plots, respectively. The Nyquist and Bode plot gives information about the real and imaginary components of impedance and the phase shift within the applied frequency range [53, 54]. Figure 8a and c represents the Nyquist plot of the substrate and clad samples at various time intervals. These plots represent a capacitive loop which proves that the electrochemical reaction is dominant during the EIS analysis [55]. Generally, the semicircular arc radius of the Nyquist plot determines the resistance against corrosion. Greater arc radius results in

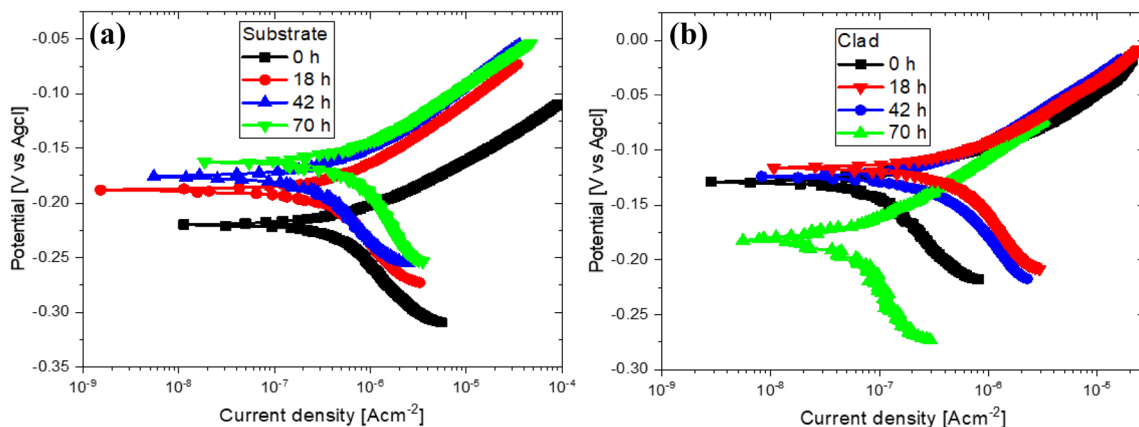


**Fig. 4** Tafel graph of: **a** Substrate and **b** clad samples at various time intervals

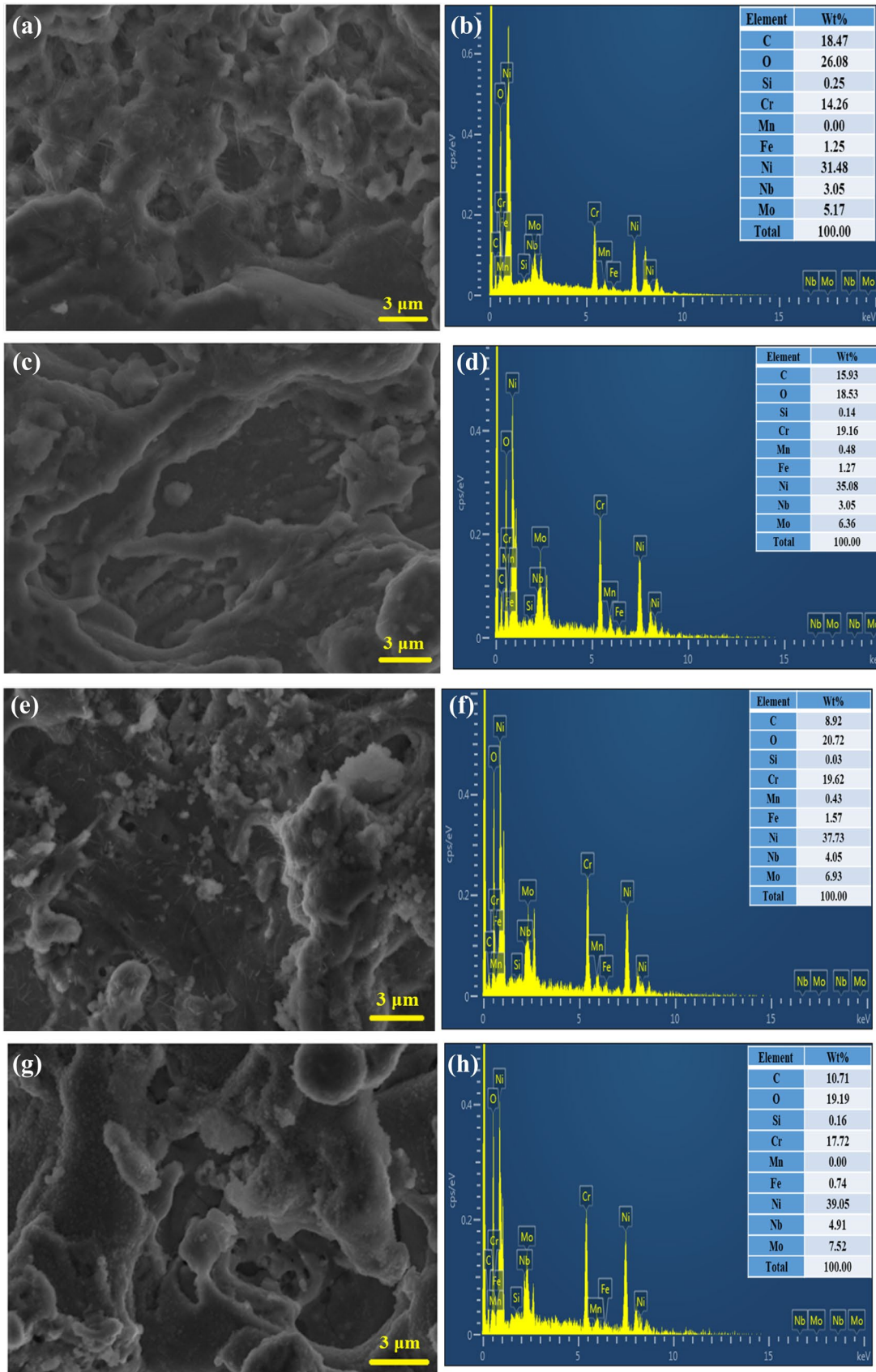


**Fig. 5** FESEM image and EDS elemental graphs of the corroded substrate samples at **a, b** 0 h, **c, d** 18 h, **e, f** 42 h and **g, h** 70 h

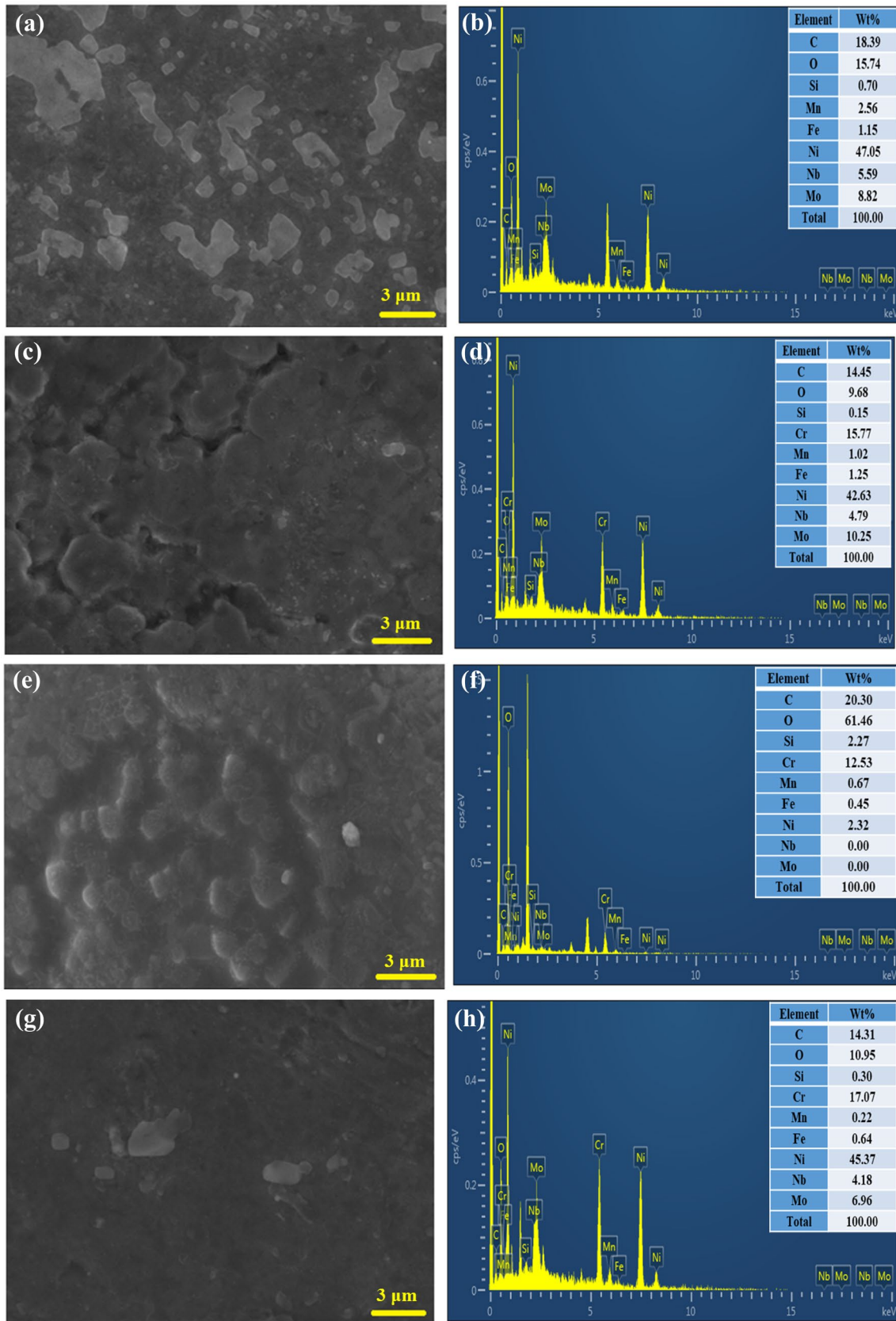


**Fig. 6** FESEM image and EDS elemental graphs of the corroded cladded samples at **a, b** 0 h, **c, d** 18 h, **e, f** 42 h and **g, h** 70 h



maximum corrosion resistance [56]. From Fig. 8a, the 70 h substrate sample has the maximum semicircular arc radius. Other substrate samples experience a decreasing trend in their arc radius. Hence, the 70 h substrate sample offers maximum resistance to corrosion among the substrate samples. On the other hand, the clad samples exhibit a higher arc radius (Fig. 8c) than the base samples. This is due to the formation of a strong passive layer containing carbide precipitates. Particularly, the unexposed clad sample provides significant resistance against corrosion since this sample has a maximum arc radius than all samples.

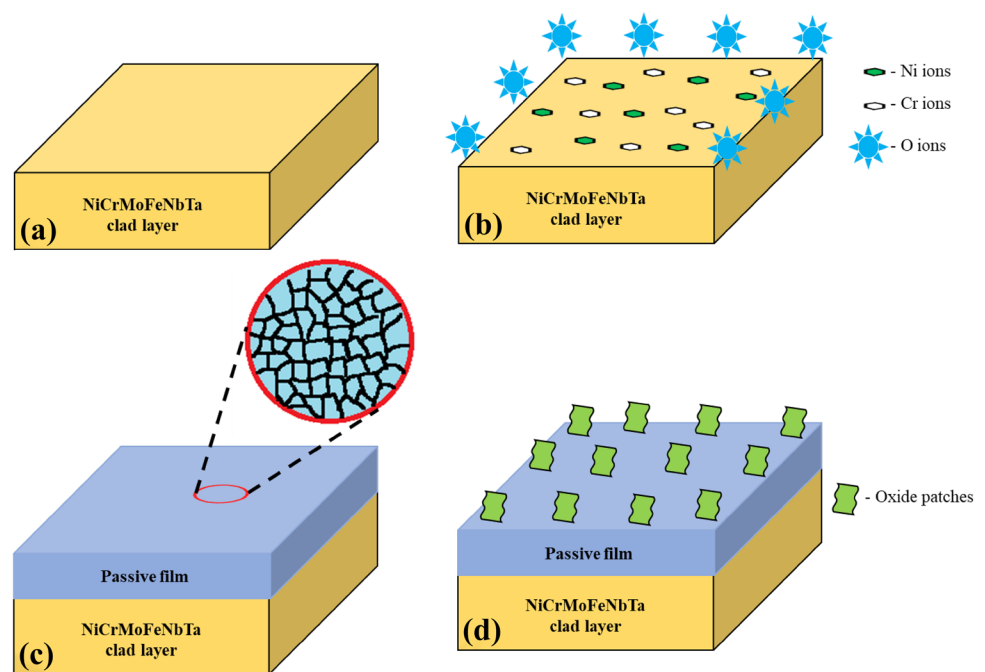
The Bode plots will evaluate the resistance characteristic via the area covered by the curves of this plot. A larger covered area results in better anti-corrosion behaviour [57]. Figure 8b represents the Bode plots of the substrate samples. It can be seen that the 70 h sample

has the maximum area covered than the 0, 18 and 42 h samples. Thus, the 70 h sample provides better resistance towards corrosion. On the other hand, all the clad samples have a better area covered than their respective substrate samples (Fig. 8d). In particular, the unexposed clad sample has a wider area coverage and offers maximum resistance against corrosion than other clad and substrate samples. In addition, with the aid of an equilibrium circuit [Inset in Fig. 8d], the polarization resistance value ( $R_p$ ) was calculated because higher  $R_p$  values result in greater corrosion resistance [58]. Table 5 lists the equilibrium circuit parameters obtained for the substrate and clad samples. Higher  $R_p$  values were noticed in the clad samples than the IN 625 substrates. Notably, the unexposed clad sample has the maximum  $R_p$  value (185,900) and provides better anti-corrosion behaviour during the corrosion process. Thus, the electrochemical

**Table 4** The elemental compositions of different specimens after corrosion test

	Element	C	O	Si	Cr	Fe	Ni	Nb	Mo	Mn	Totals
Substrate 0 h	Weight%	18.47	26.08	0.25	14.26	1.25	31.48	3.05	5.17	0.00	100.00
Substrate 18 h	Weight %	15.93	18.53	0.14	19.16	1.27	35.08	3.05	6.36	0.48	100.00
Substrate 42 h	Weight %	8.92	20.72	0.03	19.62	1.57	37.73	4.05	6.93	0.43	100.00
Substrate 70 h	Weight %	10.71	19.19	0.16	17.72	0.74	39.05	4.91	7.52	0.00	100.00
Clad 0 h	Weight%	18.39	15.74	0.70	0.00	1.15	47.05	5.59	8.82	2.56	100.00
Clad 18 h	Weight%	14.45	9.68	0.15	15.77	1.25	42.63	4.79	10.25	1.02	100.00
Clad 42 h	Weight%	20.30	61.46	2.27	12.53	0.45	2.32	0.00	0.00	0.67	100.00
Clad 70 h	Weight%	14.31	10.95	0.30	17.07	0.64	45.37	4.18	6.96	0.22	100.00

**Fig. 7** Mechanism of passivation layer formation **a** NiCr-MoFeNbTa clad layer, **b** Reaction of Ni, Cr ions in the clad layer with the O ions during the corrosion process, **c** Formation of stable passive film on the clad layer due to the effect of secondary phase and **d** As time increases, the fragile patches start to leave the surface



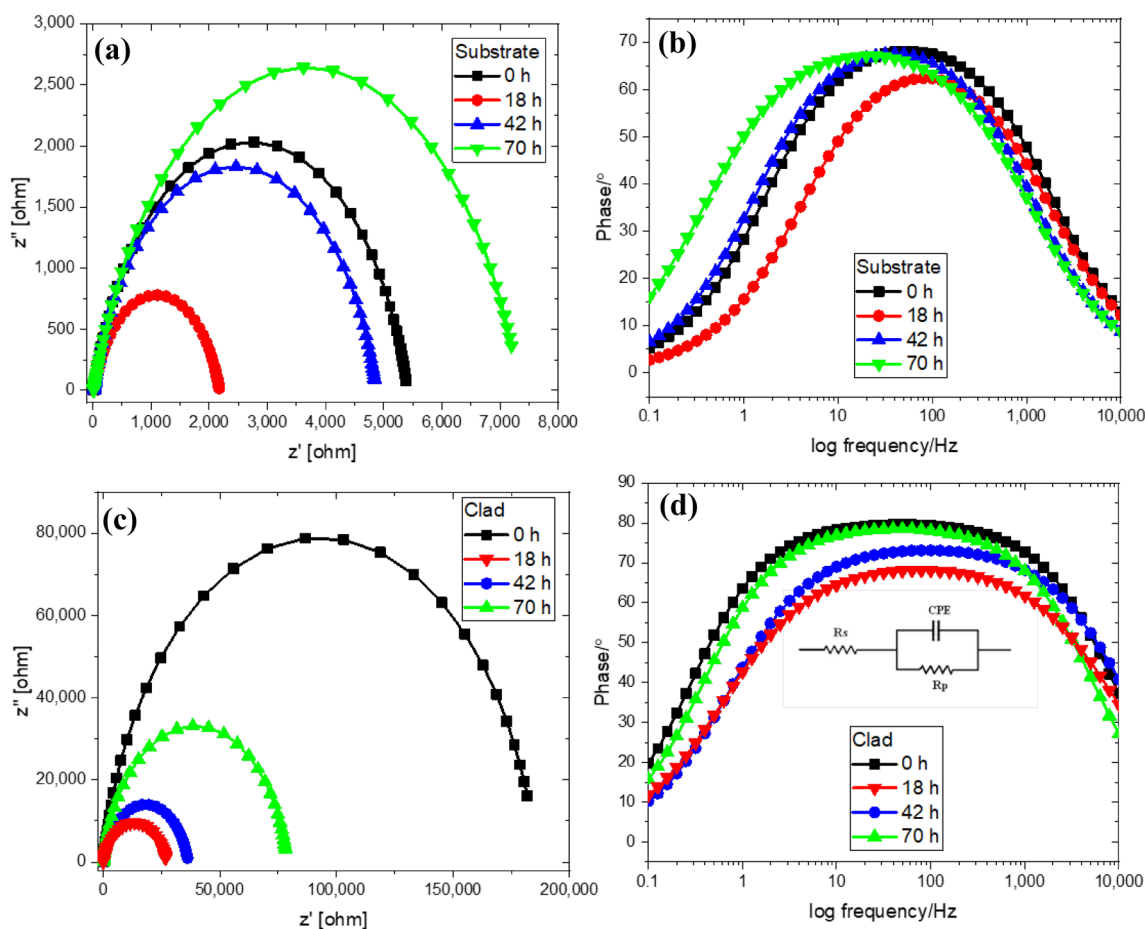


**Fig. 8** Nyquist and bode plots of different time intervals **a, b** Substrate samples, and **c, d** Clad samples

studies show the existence of the larger semicircular arc radius (Nyquist plot), wider area coverage (Bode plot) and greater  $R_p$  values in the clad samples thereby proves that the cladding process providing better resistance against corrosion.

### 3.5 Surface Roughness Examination

Surface roughness is a way of measuring the irregularities present on the surface which influences the wear resistance and corrosion rate because rough surfaces have many irregularities (interfacial sites) that are prone to corrosion attacks and reduce their resistance [59, 60]. Figure 9a–d shows the surface plot and the 2D images captured at the substrate and clad region before performing the corrosion test. The average surface roughness value ( $R_a$ ) in these regions is obtained from these images. The base region experiences a surface roughness of 29.3 nm, whereas the surface roughness at the clad region has been found to be 68.3 nm.

The clad surface has the highest value because of the deposition of NiCrMoFeNbTa alloy particles. On comparing the 2D images of base and clad samples, it is evident that the alloy particles distribution has increased the surface roughness in the clad sample. Figure 10a–d shows the 3D images captured from the substrate samples at various time intervals after the corrosion test. These figures show that the surface irregularities present in the 70 h sample are lower than that of 0, 42 and 18 h samples. In the case of clad samples, their surface seems to be rougher (Fig. 11a–d) due to the presence of precipitates of Nd- and Cr-rich carbides. In addition, the average surface roughness value ( $R_a$ ) has been calculated for the substrate and clad samples and is listed in Table 6. The lower surface roughness value results in greater resistance towards corrosion [61]. From this table, the roughness value increases as the sample's exposure time increases (18 and 42 h) and then decreases (70 h). This is due to the stability of passive film at 18 and 42 h intervals of the substrate and clad samples. At higher intervals (70 h),

**Table 5** Parameter values of different elements used in EIS analysis

Duration	Element parameter	Rs	Rp	CPE	N
		R	R	Y0	
Substrate 0 h ( $\chi^2 = 0.98456$ )	Value	16.245	5394.1	2.72E-05	0.82276
	Estimated error (%)	3.344	2.828	6.001	1.14
Substrate 18 h ( $\chi^2 = 1.7414$ )	Value	17.237	2157.4	3.51E-05	0.79735
	Estimated error (%)	4.548	3.42	10.35	1.936
Substrate 42 h ( $\chi^2 = 2.1946$ )	Value	17.965	4853.1	3.72E-05	0.82308
	Estimated error (%)	4.652	4.336	8.976	1.784
Substrate 70 h ( $\chi^2 = 1.4417$ )	Value	13.193	7326.9	6.72E-05	0.7959
	Estimated error (%)	3.786	4.175	5.722	1.265
Clad 0 h ( $\chi^2 = 1.6472$ )	Value	18.043	185,900	3.15E-06	0.89687
	Estimated error (%)	5.458	4.871	5.146	0.851
Clad 18 h ( $\chi^2 = 1.2153$ )	Value	14.161	27,154	1.26E-05	0.78448
	Estimated error (%)	5.17	3.53	5.135	0.941
Clad 42 h ( $\chi^2 = 0.9611$ )	Value	10.873	36,507	7.90E-06	0.83372
	Estimated error (%)	4.716	2.978	4.466	0.75
Clad 70 h ( $\chi^2 = 1.1773$ )	Value	16.191	78,846	5.77E-06	0.89047
	Estimated error (%)	4.11	3.428	4.527	0.776

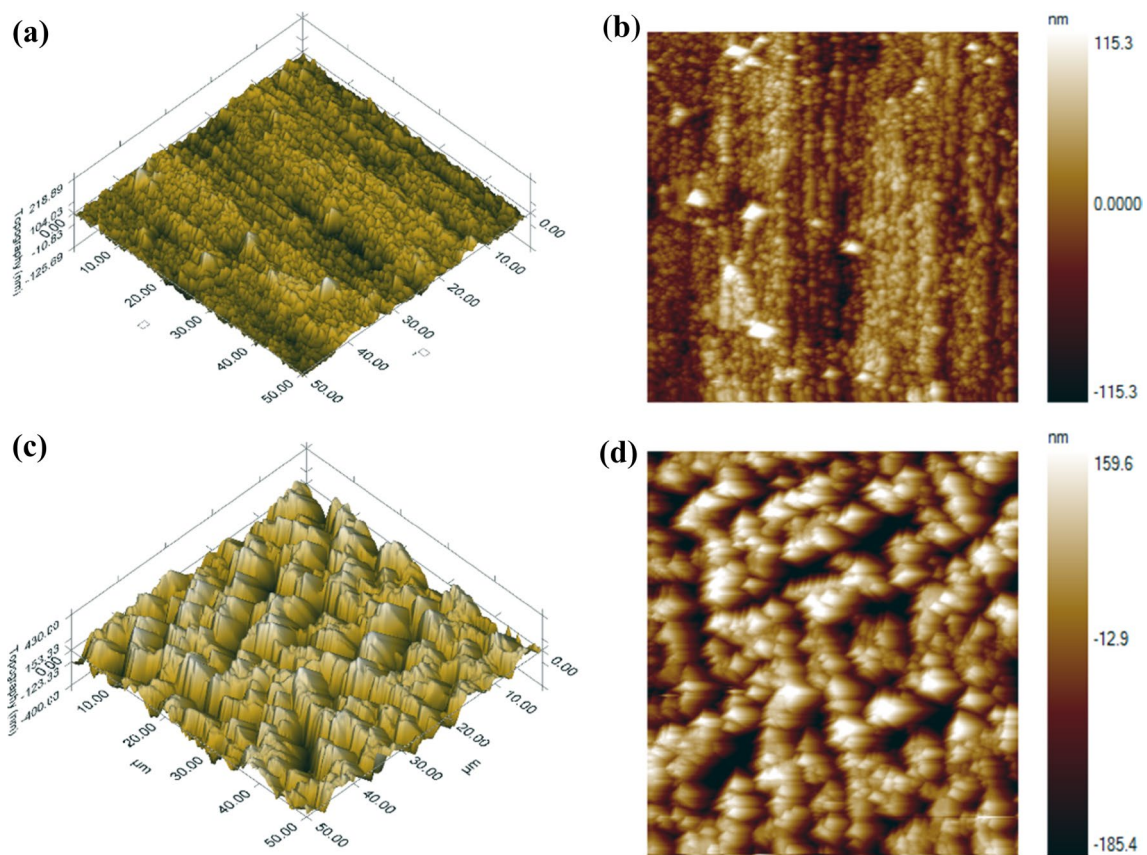


**Fig. 9** 3D surface and 2D graph SPM images of **a, b** Substrate, and **c, d** Cladded samples before corrosion test

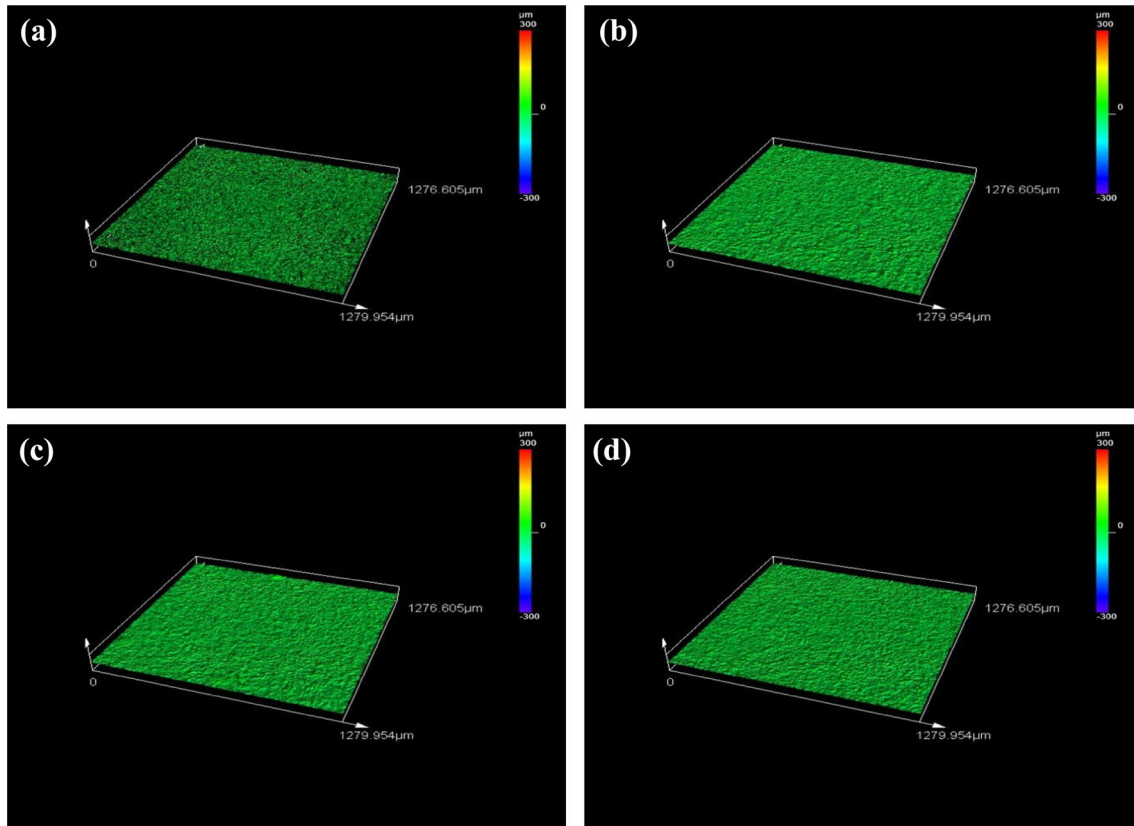


**Fig. 10** 3D surface plot obtained after the corrosion test using laser microscope for the substrate samples at **a** 0 h, **b** 18 h, **c** 42 h, and **d** 70 h

there will be fragile oxide patches on the film which pave the way for a reduction in the surface roughness value. And also from Table 6, it is seen that the 70 h substrate and the unexposed clad samples have the lowest surface roughness values ( $2.908 \mu\text{m}$  and  $6.678 \mu\text{m}$ ) and offer maximum resistance against corrosion than the other substrate and clad samples. And also, all the clad samples have higher surface roughness than the substrate. This is due to the precipitation of interdendritic secondary phases in the clad region. Hence, the clad samples offer greater corrosion resistance with increased surface roughness values.

#### 4 Conclusion

In this work, the laser cladding of NiCrMoFeNbTa alloy particles on the IN 625 substrate was performed. The characteristics of clad samples like corrosion resistance, hardness, surface roughness and the clad

microstructure were analysed and the results are summarized as given as follows:

The optical and FESEM images captured at the clad layer show the presence of cellular/dendritic structure with interdendritic secondary phases that are distributed in the  $\gamma$ -nickel matrix. Moreover, the secondary phases are rich in the carbides of niobium and chromium which alter the mechanical properties like hardness and surface roughness. The clad layer experiences a higher hardness ( $4.39 \text{ GPa}$ ) than the interface and substrate region. The clad samples have better passive film, and in particular, the unexposed clad sample provides maximum resistance as it has the minimum current density value. In addition, the clad samples have a comparatively higher  $R_p$  and  $R_a$  value and provide better corrosion resistance than the substrate samples. Thus, laser cladding of NiCrMoFeNbTa alloy particles shows improved corrosion resistance and hardness property. Hence, it is well suited for improving the working life of the components in hostile environments.

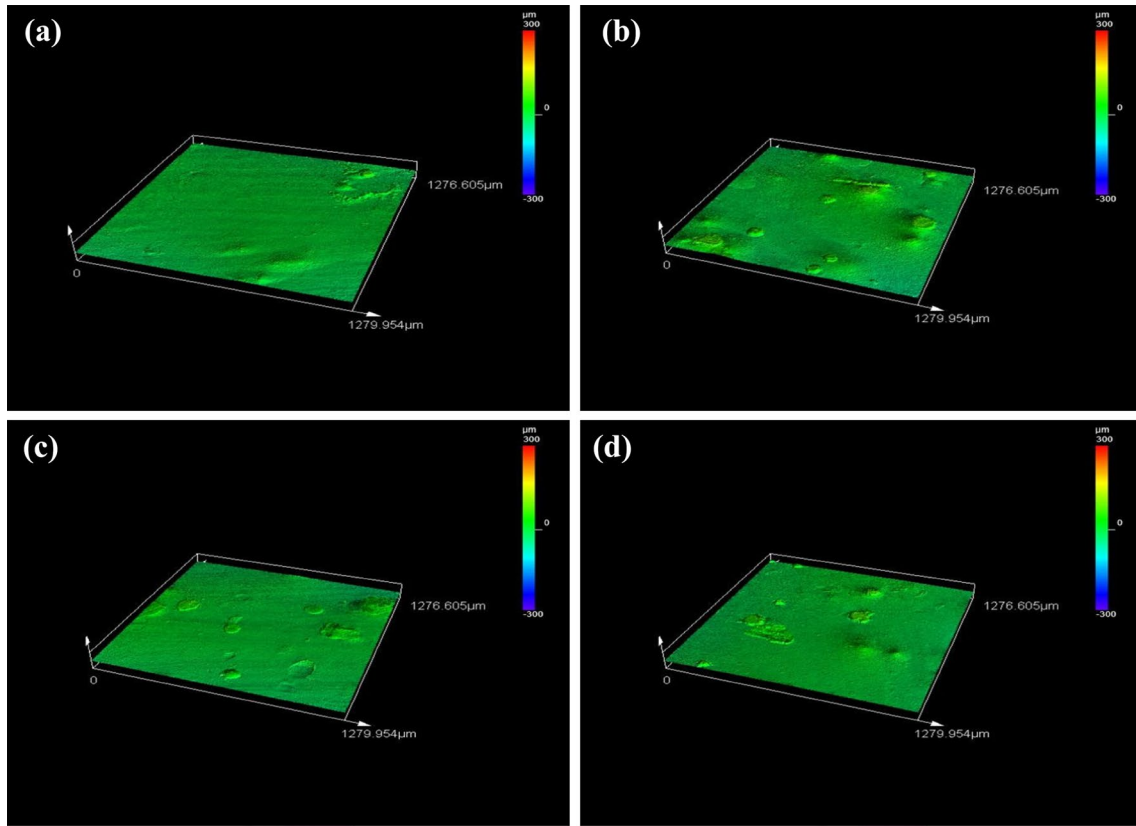


**Fig. 11** 3D surface plot obtained after the corrosion test using laser microscope for the cladded samples at **a** 0 h, **b** 18 h, **c** 42 h, and **d** 70 h

**Table 6** Roughness values (Ra) of substrate and clad samples after corrosion test

Specimens	Roughness value—Ra (μm)
Substrate 0 h	2.970
Substrate 18 h	3.161
Substrate 42 h	3.118
Substrate 70 h	2.908
Clad 0 h	6.678
Clad 18 h	12.866
Clad 42 h	8.808
Clad 70 h	8.406

**Acknowledgements** The authors would like to acknowledge the Ministry of Science and Technology, Taiwan, for granting the funds for the successful completion of this research work.

**Data Availability** The experimental datasets obtained from this research work and then the analysed results during the current study are available from the corresponding author on reasonable request.

**Declarations**

**Conflicts of interest** The authors declare that there is no conflict of interest.

**References**

1. Dong H, editor. *Surface Engineering of Light Alloys: Aluminium, Magnesium and Titanium Alloys*.
2. Holmberg K and Matthews A, *Coatings Tribology: Properties, Mechanisms, Techniques and Applications in Surface Engineering*. Elsevier, (2009).
3. Davis JR, editor. *Surface Engineering for Corrosion and Wear Resistance*, ASM international (2001).
4. Zhecheva A, Sha W, Malinov S, and Long A, *Surf Coat Technol* **200** (2005) 2192.
5. Mehran Q M, Fazal M A, Bushroa A R, and Rubaiee S, *Crit Rev Solid State Mater Sci* **43** (2018) 158.
6. Carlsson J O, and Martin P M, in *Handbook of Deposition Technologies for films and coatings*. William Andrew Publishing (2010), p. 314. <https://doi.org/10.1016/B978-0-8155-2031-3.00007-7>
7. Siddiqui A A, and Dubey A K, *Opt Laser Technol*. **134** (2021) 106619.
8. Ahn D G, *Int J Precis Eng Manuf* **14** (2013) 1271.
9. Earl C, Castrejón-Pita J R, Hilton P A, and O’Neill W, *J Manuf Process* **21** (2016) 214.
10. Singh A, and Harimkar S P, *JOM* **64** (2012) 716.

11. Mao B, Siddaiah A, Liao Y, and Menezes P L, *J Manuf Process* **53** (2020) 153.
12. Kusiński J, Kac S, Kopia A, Radziszewska A, Rozmus-Górnikowska M, Major B, Major L, Marczak J, and Lisiecki A, *Tech Sci* **60** (2012) 711.
13. Wahab J A, Ghazali M J, Yusoff W M, and Sajuri Z, *Trans IMF* **94** (2016) 193.
14. Ferreira M G, and Li R, in *Organic and Inorganic Coatings for Corrosion Prevention—Research and Experiences*, CRC Press (2019) p 194.
15. Liu Y, Ding Y, Yang L, Sun R, Zhang T, and Yang X, *J Manuf Process* **66** (2021) 341.
16. Zhong M, and Liu W, *Proc Inst Mech Eng Part C: J Mech Eng Sci* **224** (2010) 1041.
17. Jeyaprakash N, and Yang C H, *Mater Manuf Process* **35** (2020) 1383.
18. Darolia R, *Int Mater Rev* **64** (2019) 355.
19. Pollock T M, and Tin S, *J Propuls Power* **22** (2006) 361.
20. Prakash F P, Jeyaprakash N, Duraiselvam M, Prabu G, and Yang C H, *Surf Coat Technol* **397** (2020) 126055.
21. Leary M, Mazur M, Williams H, Yang E, Alghamdi A, Lozanovski B, Zhang X, Shidid D, Farahbod-Sternahl L, Witt G, and Kelbassa I, *Mater Des* **157** (2018) 179.
22. Lotfi M, Jahanbakhsh M, and Farid A A, *Tribol Int* **99** (2016) 107.
23. Abioye T E, McCartney D G, and Clare A T, *J Mater Process Technol* **217** (2015) 232.
24. Abioye T E, Folkes J, and Clare A T, *J Mater Process Technol* **213** (2013) 2145.
25. Verdi D, Garrido M A, Múñez C J, and Poza P, *Mater Sci Eng A* **598** (2014) 15.
26. Chen T C, Chou C C, Yung T Y, Tsai K C, and Huang J Y, *Surf Coat Technol* **303** (2016) 78.
27. Liu Z, Cabrero J, Niang S, and Al-Taha Z Y, *Surf Coat Technol* **201** (2007) 7149.
28. Al-Fadhli H Y, Stokes J, Hashmi M S, and Yilbas B S, *Surf Coat Technol* **200** (2006) 5782.
29. Chen T C, Chou C C, Yung T Y, Cai R F, Huang J Y, and Yang Y C, *Surf Coat Technol* **385** (2020) 125442.
30. Jeyaprakash N, Yang C H, and Ramkumar K R, *Appl Phys A* **126** (2020) 1.
31. Norhafzan B, Khairil C M, and Aqida S N, in *IOP Conference Series: Materials Science and Engineering* Vol. 1078, No. 1. IOP Publishing (2021), p 012037.
32. Geng Y, Kononov S V, and Chen X, *Usp Fiz Met* **21** (2020) 26.
33. Kwok C T, Cheng F T, and Man H C, *Mater Sci Eng A* **290** (2000) 145.
34. Fesharaki M N, Shoja-Razavi R, Mansouri H A, and Jamali H, *Surf Coat Technol* **353** (2018) 25.
35. Xu X, Mi G, Chen L, Xiong L, Jiang P, Shao X, and Wang C, *J Alloys Compd* **715** (2017) 362.
36. Rombouts M, Maes G, Mertens M, and Hendrix W, *J Laser Appl* **24** (2012) 052007.
37. Solecka M, Kopia A, Radziszewska A, and Rutkowski B, *J Alloys Compd* **751** (2018) 86.
38. Tian Y, Ouyang B, Gontcharov A, Gauvin R, Lowden P, and Brochu M, *J Alloys Compd* **694** (2017) 429.
39. Patel S J, and Smith G D, in *International Symposium on Niobium 2001* (2001), p 1081.
40. Jeyaprakash N, Yang C H, and Sivasankaran S, *Mater Manuf Process* **35** (2020) 142.
41. Konyashin I, Ries B, Hlawatschek D, Zhuk Y, Mazilkin A, Straumal B, Dorn F, and Park D, *Int J Refract Met Hard Mater* **49** (2015) 203.
42. Pharr G M, and Bolshakov A, *J Mater Res* **17** (2002) 2660.
43. Hu H X, Guo X M, and Zheng Y G, *Wear* **428** (2019) 246.
44. Badiger R I, Narendranath S, and Srinath M S, *J Manuf Process* **18** (2015) 117.
45. Mithilesh P, Varun D, Reddy A R, Ramkumar K D, Arivazhagan N, and Narayanan S, *Proc Eng* **75** (2014) 66.
46. Cozar R, and Pineau A, *Metallurg Trans A* (1973) 47.
47. Fantozzi D, Matikainen V, Uusitalo M, Koivuluoto H, and Vuoristo P, *Surf Coat Technol* **318** (2017) 233.
48. Kim H, Mitton D, and Latanision R M, in *Corrosion 2010*. OnePetro (2010).
49. Kritzer P, Boukis N, and Dinjus E, *Corrosion* **54** (1998) 824.
50. Schmuki P, Virtanen S, Davenport A J, and Vitus C M, *J Electrochem Soc* **143** (1996) 3997.
51. Ezhilselvi V, Nithin J, Balaraju J N, and Subramanian S, *Surf Coat Technol* **288** (2016) 221.
52. Sidane D, Chicot D, Yala S, Ziani S, Khireddine H, Iost A, and Decoopman X, *Thin Solid Films* **593** (2015) 71.
53. Yin Z F, Zhao W Z, Lai W Y, and Zhao X H, *Corros Sci* **51** (2009) 1702.
54. Amudha A, Nagaraja H S, and Shashikala H D, in *AIP Conference Proceedings* Vol. 2247, No. 1. AIP Publishing LLC (2020), p 040012.
55. Guo L, Zheng H, Liu S, Li Y, Feng C, and Xu X, *Int J Electrochem Sci* **11** (2016) 5507.
56. Natarajan J, Yang C H, and Karuppasamy S S, *Materials* **14** (2021) 6183.
57. Ahn S H, Choi Y S, Kim J G, and Han J G, *Surf Coat Technol* **150** (2002) 319.
58. Chira M, Hegyi A, Vermeşan H, Szilagyi H, and Lăzărescu A, *Proc Manuf* **46** (2020) 4.
59. Hagen C M, Hognestad A, Knudsen O Ø, and Sørby K, *Prog Organ Coat* **130** (2019) 17.
60. Walter R, and Kannan M B, *Mater Des* **32** (2011) 2350.
61. Jeyaprakash N, Yang C H, and Karuppasamy S S, *Surf Rev Lett* (2022).

**Publisher's Note** Springer Nature remains neutral with regard to jurisdictional claims in published maps and institutional affiliations.

Springer Nature or its licensor (e.g. a society or other partner) holds exclusive rights to this article under a publishing agreement with the author(s) or other rightsholder(s); author self-archiving of the accepted manuscript version of this article is solely governed by the terms of such publishing agreement and applicable law.